This is an *Accepted Manuscript*, which has been through the Royal Society of Chemistry peer review process and has been accepted for publication.

Accepted Manuscripts are published online shortly after acceptance, before technical editing, formatting and proof reading. Using this free service, authors can make their results available to the community, in citable form, before we publish the edited article. We will replace this *Accepted Manuscript* with the edited and formatted *Advance Article* as soon as it is available.

You can find more information about *Accepted Manuscripts* in the **Information for Authors**.

Please note that technical editing may introduce minor changes to the text and/or graphics, which may alter content. The journal's standard **Terms & Conditions** and the **Ethical guidelines** still apply. In no event shall the Royal Society of Chemistry be held responsible for any errors or omissions in this *Accepted Manuscript* or any consequences arising from the use of any information it contains.

Journal Name

ARTICLE

Solid solubility of rare earth elements (Nd, Eu, Tb) in $In_{2-x}Sn_xO_3$ - effect on electrical conductivity and optical properties

T.O.L. Sunde,[a] M. Lindgren,[b] T.O. Mason,[c] M.-A. Einarsrud[a] and T. Grande[a*]

Wide band-gap semiconductors doped with luminescent rare earth elements (REEs) have attracted recent interest due to their unique optical properties. Here we report on the synthesis of the transparent conducting oxides (TCOs) indium oxide and indium tin oxide (ITO) doped with neodymium, europium and terbium. The solid solubility in the systems was investigated and isothermal phase diagrams at 1400 °C were proposed. The solubility of the REEs in In_2O_3 is mainly determined by the size of the rare earth dopant, while in ITO the solid solubility was reduced due to a strong tendency of the tin and REE co-dopants to form a pyrochlore phase. The effect of the REE-doping on the conductivity of the host was determined and optical activity of the REE dopants were investigated in selected host materials. The conductivity of sintered materials of REE-doped In_2O_3 was significantly reduced, even at small doping concentrations, due to a decrease in carrier mobility. The same decrease in mobility was not observed in thin films of the material processed at lower temperatures. Strong emissions at around 611 nm were observed for Eu-doped In_2O_3, demonstrating the possibility of obtaining photoluminescence in a TCO host, while no emissions was observed for Nd- and Tb-doping.

Introduction

The rare earth elements (REEs) or lanthanides are known for their characteristic luminescence and have found many applications due to their unique optical properties.[1-5] The REE activators are usually efficient emitters of light once they are in the excited state, yet often ineffective at absorbing energy in the first place, due to parity forbidden 4f-4f transitions and small optical absorption cross-sections, which can severely limit their efficiency.[1,2] In applications based on organic or inorganic-organic hybrid materials appropriate energy transfer from ligands or dendritic shells can be used to activate the luminescent lanthanide ion.[6-9] It has therefore recently become attractive to use wide band gap semiconductors as host materials for the REE activators.[10] Similar to the organic ligands, these hosts have the possibility to absorb UV light with energy higher than the band gap of the material and transfer the energy to the REE activator, thereby sensitising the luminescence. The possibility of this energy transfer, often referred to as host sensitisation, has been a major driving force for the use of wide band gap hosts such as In_2O_3,[11] Al_2O_3,[12] ZnO,[13-17] TiO_2,[18-20] ZrO_2[21] and SnO_2.[22,23] It is proposed that such phosphors can be used in applications such as upconversion phosphors for solar cells, light-emitting diodes, displays, lasing, bioimaging, optoelectronics or others.[10,11,24-27]

In_2O_3 might be a potentially good host material for a REE dopant, as all the rare earth sesquioxides crystallise in the same bixbyite crystal structure as In_2O_3.[28] Additionally, all of the REEs are usually trivalent with sizes relatively similar to that of In^{3+}.[29] This indicates that the solid solubility of REEs in In_2O_3 could be sufficient to avoid concentration quenching of the luminescence or the formation of secondary phases which are not optically active. Furthermore, In_2O_3, particularly when it is doped with tin to form indium tin oxide (ITO), is known to be a transparent conducting oxide (TCO) with excellent properties.[30-33] On the other hand, most host materials for REE phosphors have traditionally been glasses or other electric insulators.[1,34-36] A multifunctional material with the combination of being luminescent while retaining a good conductivity and transparency could be realized by using a TCO as a host. This could potentially open up to new possibilities, for instance for applications based on electro-luminescence,[1,3] which has motivated studies of ITO doped with REEs.[25,26,37] From a fundamental point of view it is of interest to investigate whether the REEs can be optically active in In_2O_3 or ITO, but also to which extent the doping affects the functional properties of the

host, where the latter has received significantly less attention in the literature.

The majority of the work concerning REE-doping of indium oxide-based hosts has used Eu^{3+} as the activator,[11,12,24] although also Er^{3+},[25,38,39] Nd^{3+},[40] Tb^{3+},[41] and Dy^{3+},[27] have been applied. In most of these studies undoped In_2O_3 has been used as the host, but in a few cases tin-doping to prepare ITO has been attempted.[25,26,37] The final state of the materials is also varying, ranging from nano-crystalline[24] to sub-micron[11] powders to thin films on different substrates.[12,25,26,38,42] In some cases an optically inert matrix has been used into which Eu^{3+} and In_2O_3 nanoparticles have been co-doped.[43-45] There is some degree of discrepancy in the literature regarding the energy transfer from the host to the activator, called the host sensitisation. In fact, in some of the cases emission signals could only be obtained under direct excitation of the energy levels of the activator,[25,27] whereas in another case emissions were only observed upon excitation over the band gap of the host, and direct excitation was not possible.[38] However, it seems to be clear that an energy transfer from In_2O_3 to a REE is achievable.[11,40,41,43,44]

The solubility limit of the REE activators in In_2O_3 and the amount of doping that can be used before concentration quenching of the emissions occurs remains unclear. When Er was added to ITO, no concentration quenching was observed up to at least 5 cat %,[25] but a recent work by Ting et al. observed concentration quenching from Eu in ITO already above 0.1 cat %.[37] On the other hand, Vela et al. observed maximum emissions when 15 to 30 cat % Eu was doped into nano-particles of In_2O_3.[24]

In this work we report on the synthesis of In_2O_3 and ITO doped with neodymium, europium and terbium by an aqueous sol-gel process. The first part of the paper focuses on the solid solubility of the dopants and isothermal phase diagrams at 1400 °C are presented. The second part is devoted to the functional properties of the materials. The electrical properties of the materials were characterised by conductivity and thermopower measurements in order to determine to which extent the REE-doping affected the conductivity of the host. The characterisation of the optical properties, measured by diffuse reflectance and photoluminescence spectroscopy, was performed in order to verify if the REE dopants could be optically active in the selected host materials.

Experimental

Materials synthesis

A water-based modified Pechini sol-gel process was used to synthesise the materials, previously developed for synthesis of indium tin oxide.[46] Indium (III) nitrate hydrate ($In(NO_3)_3 \cdot xH_2O$), tin (II) acetate ($Sn(CH_3CO_2)_2$), neodymium (III) nitrate hexahydrate ($Nd(NO_3)_3 \cdot 6H_2O$), europium (III) nitrate pentahydrate ($Eu(NO_3)_3 \cdot 5H_2O$) and terbium (III) nitrate pentahydrate ($Tb(NO_3)_3 \cdot 5H_2O$) (all > 99.9 % trace metals basis, from Aldrich) were

used as precursors. The stoichiometry of indium nitrate (water content) was determined by thermogravimetric analysis prior to the syntheses.

The following materials were prepared: In_2O_3, In_2O_3 doped with 5 cat% Sn (ITO), In_2O_3 doped with 0.5, 1, 2, 5 and 10 cat% RE (RE = Nd, Eu or Tb) and ITO doped with 1, 5 and 10 cat% RE. The ratio between indium and tin was kept constant at 95:5 in REE-doped ITO. The compositions are summarised in Table 1.

Stoichiometric amounts of the precursors were dissolved in de-ionised water and heated to about 80 °C on a hot plate with a magnetic stirrer. Tartaric acid (TA, DL-tartaric acid, 99 %, Sigma-Aldrich) and ethylene glycol (EG, $C_2H_4(OH)_2$, VWR) were added to the solution as complexing agents, in a molar ratio between the cations in the solution and each of the organics of 1:1.5. The sol was left on the hot plate overnight in order to evaporate the solvent and form a xerogel. All of the gels were demonstrated by XRD to be amorphous. The as-prepared gel was ground in a mortar and calcined at 600 °C for 15 h, in order to decompose the gel to a nano-crystalline oxide powder. The calcined oxide powder was then ball milled with 5 mm YSZ balls in absolute ethanol for 24 h in order to remove possible hard agglomerates. Pellets of the ball milled powders with 15 mm diameter and about 2.5 mm height were pressed by uniaxial pressing at < 50 MPa, followed by subsequent cold isostatic pressing at 200 MPa. Stearic acid was used as a lubricant during the pressing of the pellets. The pressed pellets were sintered for 2 h in air 1400 °C. The heating and cooling rates were 200 °C/h. The density of the sintered materials was determined by the Archimedes method. When the term nano-crystalline powder is used it refers to the prepared powders which were calcined at 600 °C, while the term sintered materials refers to the samples after sintering at 1400 °C.

Thin films of selected compositions were also deposited by spin coating of the aqueous precursor solution on glass substrates. Details about the deposition have been described elsewhere.[46] Acetic acid (p.a. Acros Organics) and ethylene glycol were used as complexing agents and about 1.5 wt% PVA (VWR, average $M_w \approx$ 88000 g/mol), was added as a wetting agent for the solutions used for spin coating. Their cation concentration was 0.4 M. The films were prepared by three subsequent depositions, with a subsequent calcination under vacuum (10^{-2} mbar) in a rapid thermal processing furnace (RTP, Jipelec JetFirst 200 Processor) at 530 °C for 1 h after each deposition.

Materials characterisation

The materials were analysed by X-ray powder diffraction (XRD) on a Siemens D5005 instrument with an MBraun position sensitive detector, Cu-radiation source ($CuK\alpha_1$), primary monochromator and Bragg Brentano geometry. The step size was 0.03878 ° and the counting time was 7.3 s per step. The sintered pellets were crushed before the sample preparation. XRD of the thin films were performed on a Siemens D5005 with a

gracing incidence angle set-up, Cu-radiation source ($CuK\alpha_{1,2}$), Göbel mirror, equatorial soller slits on the detector side and a Scintillation detector. The incident angle was set at 2 °, and the films were analyzed from 20 to 70 °2θ with an incremental step of 0.08 ° and a counting time of 7.3 s per step. Rietveld refinements of the diffractograms were carried out using the Topas software, v4.2. The crystal structure of the materials, including the position of the atoms in the unit cell, was refined using the space groups $Ia\overline{3}$ for cubic bixbyite In_2O_3,[47] $Fd\overline{3}m$ for the rare earth stannate pyrochlore phases $RE_2Sn_2O_7$ (RE = Nd, Eu and Tb),[48,49] $Pnma$ for $NdInO_3$[50,51] and $P6_3cm$ for $EuInO_3$ and $TbInO_3$.[52,53] The crystallite size of the powders was analysed by diffraction line broadening and the Scherrer equation.

Scanning electron microscopy (FEG-SEM, Zeiss Ultra 55 Limited Edition) was performed on the top view of the thin film surfaces.

The conductivity (with a four point linear probe configuration) and thermopower of the sintered materials were measured at ambient conditions by methods described in detail by Hong et al.[54] The calculated conductivities were corrected for the geometry of the sample as outlined by Smits et al.,[55] and for porosity by the Bruggemann symmetric model.[56] The sheet resistance of the thin films was measured by the van der Pauw method [57] (Ecopia HMS-3000). This experiment was combined with a Hall effect measurement using a 0.55 T magnet to provide the magnetic field. The experiments were performed under ambient conditions.

Diffuse reflectance spectroscopy was carried out on the sintered materials on a Perkin Elmer Lambda 1050 UV/Vis/NIR spectrophotometer with an integrating sphere detector (Perkin Elmer, Oak Brook, Il). Spectra were taken from 300 to 2500 nm, and two baseline spectra, one at 0% R and one at 100% R, were taken using pressed polytetrafluoroethylene (PTFE) powder compacts. Transmission and reflectance spectroscopy was also performed on the thin films with the same equipment. Time-resolved fluorescence decays were recorded using an IBH 5000 U fluorescence lifetime spectrometer system with excitation and emission monochromators (5000 M). The resolution could be varied between 1 and 32 nm and typically 1-6 nm were used for wavelengths scans, and 6-32 nm were used for time decays. An IBH 5000 XeF sub-microsecond xenon flashlamp was used for multi-channel scaling (MCS) measurements. The system was equipped with a TBX-04 picosecond photon detection module for detection in the UV/visible and a Hamamatsu NIR PMT module (H9170-5) for detection in the range 900–1700 nm. Melles Griot coloured glass filters were used to block scattered light from the excitation source as well as blocking unwanted light from the laser source. The luminescence decay times were measured and analysed using multi-channel scaling (MCS) along with the IBH Data Station v 2.1 software for operation of the spectrometer and analysis of the decay traces including reconvolution-fits. Luminescence spectra were collected by a lens coupled to an optical fiber and analysed by a Hamamatsu Photonic Multichannel Analyzer (type C7473).

Results

Synthesis and solid solubility

In_2O_3 host All the powders of In_2O_3 doped with different amounts of Eu, Nd and Tb were demonstrated to be nano-crystalline and appeared to be phase-pure by XRD, as shown for In_2O_3:10%Eu in the bottommost diffractogram in Fig. 1. All of the diffraction lines could be ascribed to cubic In_2O_3 with the bixbyite crystal structure (space group $Ia\overline{3}$), and the reflections were broad, demonstrating the nano-crystalline nature of the powders.

XRD patterns of sintered materials of In_2O_3 doped with different amounts of Eu after heat treatment at 1400 °C are also included in Fig. 1. At low doping concentrations the materials were phase-pure, while a secondary phase appeared at higher doping concentrations. Similar observations were made for sintered materials of In_2O_3 doped with Nd and Tb, but the amount of doping that was required for the secondary phase to appear was different for the three dopants. The diffraction lines due to the secondary phase could be ascribed to $EuInO_3$ and $TbInO_3$ with the hexagonal $YMnO_3$ crystal structure (space group $P6_3cm$) in the case of Eu- and Tb-doped materials. For Nd-doping the secondary phase was identified as $NdInO_3$ with the orthorhombic $GdFeO_3$ perovskite structure (space group $Pnma$). No traces of the rare earth oxides were observed. The phase fractions of In_2O_3 and $REInO_3$ for the different materials are given in Table 2.

The lattice parameters and crystallite sizes of the cubic In_2O_3 phase, determined for the nano-crystalline powders and sintered materials, are also included in Table 2, with the lattice parameters also being shown in Fig. 2. The lattice parameter of all materials appears to follow Vegard's law[58] at lower doping levels, while the lattice parameter saturated at higher dopant concentrations. The inflection point corresponds to the solid solubility limit of RE_2O_3 in In_2O_3 and correlates with the appearance of secondary phases, as shown in Table 2. The lattice parameters for the nano-crystalline powders followed the same trend, even though no secondary phases could be observed by XRD. Furthermore, the nano-crystalline powders seem to have larger lattice constants than the sintered materials. This difference was most noticeable for the samples doped with Nd, where the lattice constant of the nano-crystalline powder on average was about 0.018 Å larger than the sintered material, while for Eu the average difference was 0.008 Å. The Tb-doped nano-crystalline powder had larger lattice constants at small doping concentrations, which did not increase according to Vegard's law, like observed for the sintered material. The crystallite size appeared to decrease with increasing amount of REE-doping in the nano-crystalline powder.

ITO host The powders of ITO doped with Nd, Eu and Tb were also demonstrated to be nano-crystalline and appeared to be phase-pure by XRD, as shown for ITO:10%Nd in Fig. 3. All of the diffraction lines could be ascribed to cubic bixbyite In_2O_3. When different complexing agents were used in the synthesis, also the metastable rhombohedral corundum structure of In_2O_3 (space group $R\bar{3}c$) could be observed, which is further discussed in Electronic Supplementary Information (ESI). All the powders and materials discussed here were prepared from syntheses which yielded phase-pure cubic In_2O_3 powders after calcination at 600 °C. Several different phases were observed when the doped ITO materials were sintered at 1400 °C, illustrated by XRD of ITO with 1, 5 and 10 cat% Nd-doping, included in Fig. 3. For the samples with 1 and 5 cat% Nd-doping, the secondary phase was found to be a pyrochlore phase, $Nd_2Sn_2O_7$ (space group $Fd\bar{3}m$), while for the material with 10 cat% Nd-doping also the orthorhombic perovskite, $NdInO_3$, was observed. Similar observations were made for the ITO:Eu and ITO:Tb systems. The phase content for the ITO-based materials after heat treatment at 1400 °C, based on Rietveld refinement, is given in Table 3. The three different systems had approximately the same amount of the $RE_2Sn_2O_7$ pyrochlore phase for 1 and 5 cat% REE-doping, but the amount of the $REInO_3$ phase observed at 10 cat% REE-doping was smaller for Eu and Tb, thereby correlating with the observations for the pure In_2O_3 host (Table 2).

The lattice parameters and crystallite size of cubic In_2O_3 in the nano-crystalline powders and sintered materials of the doped ITO materials are also given in Table 3 and in Fig. 4. The ITO-based materials did not follow Vegard's law like the In_2O_3-based materials, which is reasonable due to a significant higher content of secondary phases and lower solid solubility. The sintered materials had similar phase contents at 1 and 5 cat% REE doping, and the lattice parameters for these materials are in close agreement. The lattice parameters of sintered samples with 10 cat% REE, on the other hand, were inversely proportional to the amount of the $REInO_3$-phase. The materials with 5 and 10 cat% REE had a higher lattice parameter than the ITO with 5 cat% Sn reference, suggesting that there is a certain solubility of REEs in ITO. On the other hand, for the sintered materials with 1 cat% REE the lattice parameter was lower than the ITO reference. The powders did not display a clear relationship between the lattice parameter and composition, but the highest lattice parameter for all three systems was observed for 10 cat% REE. The powders were all nano-crystalline with similar crystallite sizes. The $REInO_3$ phase was formed at lower temperatures than the pyrochlore $RE_2Sn_2O_7$ phase, and the phase evolution after heat treatment at different temperatures is further discussed in ESI.

Thin films Thin films of selected compositions were successfully deposited by spin coating of the aqueous precursor solution. The thin films were dense and single phase according to XRD. Details about the structural and microstructural properties of the thin films are given in ESI.

Functional properties

Electrical Properties The electrical conductivity and thermopower of sintered materials of In_2O_3 and ITO doped with the REEs are given in Fig. 5 and in Table S3. The density of the materials after sintering at 1400 °C is also included in Table S3, and the variations in density and their effect on the measured conductivities are discussed in ESI. The conductivity of ITO with 5 cat% Sn was 6145 S/cm, whereas the conductivity of In_2O_3 was 130.8 S/cm. All of the REE-doped materials had a lower conductivity than their respective hosts. The In_2O_3-based materials had a drastic decrease in conductivity even at small doping concentrations. The conductivity of 1 cat% Nd-doped In_2O_3 was nearly four orders of magnitude lower than for pure In_2O_3. The decrease was progressively smaller for Eu- and Tb-doping, but also in the latter case the decrease in conductivity from pure In_2O_3 to the material with 2 cat% Tb-doping was more than one order of magnitude. The ITO:1%REE materials had conductivities between 4180 and 5375 S/cm. The 1 cat% doped materials were not phase-pure, and it was not attempted to measure the conductivity on ITO-based materials with higher doping concentrations. The Seebeck coefficients of ITO and In_2O_3 were -30.43 and -130.8 μV/K, respectively. The negative sign of the thermopower confirms the n-type conductivity, in line with expectations.[59] The REE-doping did not appear to affect the thermopower in the same way as the conductivity. The thermopower of the In_2O_3-based materials appeared to be quite stable up to 2 cat% REE-doping, although the In_2O_3:0.5%Eu and In_2O_3:0.5%Tb materials had a somewhat lower thermopower. Also the ITO-based materials had a thermopower roughly equal to the ITO host reference.

The sheet resistance, mobility and carrier concentration of the prepared thin films are given in Fig. 6 and in Table S2. The electrical properties of the ITO-based films are largely unaffected by the REE-doping, although a slight increase in the sheet resistance can be observed at 10 cat% Eu-doping. The properties of the In_2O_3-based films were also not significantly affected at low doping concentrations, but a dramatic increase in the sheet resistance was evident at high concentrations of the REE-dopant.

Optical properties The diffuse reflectance spectra of sintered materials of In_2O_3 doped with Nd, Eu and Tb are shown in Fig. 7. The spectrum of pure In_2O_3 is given as a reference. In_2O_3 exhibited typical semiconductor behaviour with the reflectance decreasing rapidly with decreasing wavelength starting from about 500 nm due to absorptions across the band gap. The Eu-doped materials exhibited absorption in the visible region, around 530 and 580 nm, and in the IR region, at approximately 1970, 2090 and 2180 nm. The absorptions in the visible region increased with

increasing doping concentration, with the 530 nm absorption being observed for all concentrations. The absorptions in the IR-region could only be established for the In_2O_3:5%Eu material. All of the Tb-doped materials appeared to have a broad absorption from about 500 to 800 nm compared to pure In_2O_3, with increasing intensity with increasing doping concentration. Absorption lines could also be seen in the IR region for the samples with 5 and particularly 10 cat% Tb-doping. The Nd-doped materials demonstrated strong absorption bands in the region from approximately 500 to 900 nm, which appeared to increase in intensity with increasing amount of doping. Outside of this region no differences were observed between the doped materials and the In_2O_3 reference. The ITO-based materials demonstrated very low reflectance and are not reported here. The transmittance and reflectance of the thin films are reported in ESI together with the band gaps of the sintered materials and the thin films.

Photoluminescence experiments performed on the sintered materials show strong emissions for In_2O_3 doped with Eu, yet no emissions were observed for In_2O_3 doped with Nd or Tb. The excitation and emission spectra of In_2O_3:5%Eu are shown in Fig. 8 (a) and (b). When monitoring the characteristic red emission of Eu^{3+} at around 611 nm,[24] two broad excitation peaks were observed centred around 465 and 530 nm, where the intensity was highest at 530 nm. This wavelength corresponded well with the absorption observed by diffuse reflectance. No excitations were found at lower wavelengths. The emission spectra after excitation at these two wavelengths clearly shows the emission centred around 611 nm. This emission was strongest for excitation at 530 nm, in line with the intensities in the excitation spectrum. Also emissions with lower intensity were observed at approximately 578, 584, 592, 597 and 629 nm, for both excitation wavelengths. The emission at 611 nm was clearly observed for the material with 5 and 10 cat% Eu-doping, with the strongest emission for 5 cat %, but was also observed for doping concentrations as low as 1 cat% (Fig. 8 (c)).

Photoluminescence measurements were also performed on pressed porous pellets of the nano-crystalline powders. The nano-crystalline powder materials also exhibited the emission at 611 nm upon excitation at 465 and 530 nm, but with significantly lower intensity than the corresponding sintered materials. The emission was only observed for 5 and 10 cat% Eu, again with 5 cat% Eu giving the highest intensity. No experiments were performed on the ITO-based materials due to their limited solid solubility.

Luminescence decay results performed on the emission at 611 nm after excitation at 530 nm, given in Fig. 9, clearly demonstrates the different behaviour of the nano-crystalline powder and sintered materials. The lifetime of sintered In_2O_3:10%Eu appears to be approximately twice that of the corresponding nano-crystalline powder. The time decay of the sintered material appears to be close to a single exponential, as demonstrated by the nearly straight line in the logarithmic plot. The decay appears to be more complex for the nano-crystalline powder sample. Similar observations were also observed for In_2O_3:5%Eu. The decay times of nano-crystalline powders and sintered materials of In_2O_3 doped with 5 and 10 cat% Eu are summarised in Table S4. The average lifetime of the material, accounting for the relative strength of the contributions from the different decays, are given as the weighted average. The decay of the nano-crystalline powder materials were fitted by three exponential decays, while two decays were used for the sintered samples. The lifetimes corresponded well with the observed intensities in the emissions, as the materials with 5 cat% Eu had longer lifetimes than the materials with 10 cat% Eu, and that the nano-crystalline powders had a shorter lifetime than the corresponding sintered material. The lifetimes of sintered In_2O_3 doped with 5 and 10 cat% Eu were 0.867 and 0.782 ms, respectively. These life-time values are similar to those reported for organic Eu^{3+} cyclen complexes.[60]

Discussion

Synthesis and solid solubility

The equilibrium solubility of REEs in In_2O_3 could be established after annealing at 1400 °C. The solid solubility at this temperature was observed to be about 1, 5 and 10 cat% for Nd, Eu and Tb, respectively. At higher doping concentrations a secondary $REInO_3$ phase was observed (space group *Pnma* for $NdInO_3$ and *P6₃cm* for $EuInO_3$ and $TbInO_3$), while no traces of the rare earth oxides could be found. As the REEs are known to be chemically similar, the property of the dopants which is most important for their solid solubility is their size. The size of the different cations (for coordination number 6) are 80 pm for In^{3+} and 98, 95 and 92 pm for Nd^{3+}, Eu^{3+} and Tb^{3+}, respectively.[29] All of the dopants are larger than In^{3+} and the larger dopant and the size mismatch, the smaller the solid solubility. The size of the cations decreases from left to right in the lanthanide group. Hence, it is proposed that the solid solubility of the cations to the left of Nd, such as La^{3+} and Pr^{3+}, would be very small. On the other hand, cations smaller than Tb^{3+}, like the technologically important Er^{3+},[1,61] which could have good upconversion properties,[4,39] is suggested to be high. When ITO was used as a host, the solid solubility was reduced due to a strong tendency of the tin and REE co-dopants to form a pyrochlore $RE_2Sn_2O_7$ phase.

Constructed ternary isothermal phase diagrams of the In_2O_3-SnO_2-RE_2O_3 system based on the phase compositions and solid solubility limits for the bulk materials are given in Fig. 10 (a). The phase diagrams include the phases $REInO_3$, $RE_2Sn_2O_7$ and $In_4Sn_3O_{12}$, where the latter was not detected here, but is reported to be thermodynamically stable at 1400 °C.[62] The solid solubility in In_2O_3, marked with bold red lines in the bottom left corner of the phase diagram, is of most importance in this work. Based on mass balance and the

lever rule, the composition of the cubic In_2O_3 phase could be estimated, and these values are given in Table 4. It was assumed that there was no solid solubility in either $REInO_3$ or $RE_2Sn_2O_7$. Close-ups of the indium-rich corner of the phase diagrams for the three different systems are given in Fig. 10 (b), (c) and (d). The crosses represent the compositions from Table 4, together with the solid solubility of REEs in In_2O_3 and the solid solubility of Sn in In_2O_3. The latter value was 3 cat% based on the phase-diagrams of Gonzãles et al.[63] and Heward and Swenson.[64] The proposed solid solubility lines were drawn based on these points.

The most important difference between the phase diagrams in Fig. 10 (b), (c) and (d) is the solubility of the REEs in In_2O_3, which was shown to be inversely proportional to the size difference between In^{3+} and the RE^{3+}. The two-phase region between In_2O_3 and $RE_2Sn_2O_7$ increases with increasing solubility of RE in In_2O_3 at the expense of the three phase region where also $REInO_3$ is present. This correlates with the phase content of the 10 cat% REE-doped materials (Table 3). The composition of the materials with 1 and 5 cat% REE was similar for the three dopants, due to the formation of the pyrochlore $RE_2Sn_2O_7$ phase and the fixed solubility of tin in In_2O_3.

The solid solutions of all In_2O_3-based materials appeared to follow Vegard's law, except for the nano-crystalline Tb-doped powders. Also in this case the lattice parameter increased with the amount of doping, but less than expected from Vegard's law. For 5 and 10 cat% Tb the lattice parameter was notably smaller than for the sintered materials with the same composition. Terbium is known to be stable also in a tetravalent state,[28] forming TbO_2 for which the lattice parameter is smaller than the sesquioxide.[65] It is therefore proposed that a fraction of the terbium dopant being tetravalent is the cause of the relatively small lattice parameters. At small doping levels this effect was not observed, so it appears that the tetravalent fraction increased with increasing Tb-doping. After the materials were heat treated at 1400 °C this effect was not observed, as the lower oxidation state becomes more stable with increasing temperatures.[66] Tetravalent cations may work as n-type donors in In_2O_3 and the conductivity of the material may by controlled by the amount of Tb^{4+}. However, more work is needed to understand the role of varying the Tb^{3+}/Tb^{4+} ratio plays in the free carrier concentration in In_2O_3, particularly when used as a co-dopant together with tin. Furthermore, it is not known whether the luminescent ability of terbium will be retained in its tetravalent state.

It is well known that the amount of tetravalent tin in ITO affects the oxygen stoichiometry and thereby also the lattice parameter of this material.[59] It has previously been demonstrated that the lattice parameter of undoped In_2O_3 and ITO with 5 cat% Sn powders prepared by the same synthesis is 10.121 and 10.123 Å respectively.[46] When ITO is substituted with 10 cat% REE the nominal Sn-content is reduced from 5 to 4.5 cat% and the actual tin concentration in In_2O_3 is further lowered by the precipitation of the pyrochlore phase. This would cause

a decrease in the cubic lattice parameter of In_2O_3. In contrast, the ITO:10%RE nano-crystalline powders were demonstrated to have a lattice parameters ranging from 10.148 to 10.157 Å. The incorporation of the larger REEs in the lattice is dominating over the reduced tin concentration and the possible change in the oxygen stoichiometry.

All of the prepared nano-crystalline powders appeared to be phase-pure based by XRD. However, similarly as for the sintered materials, the nano-crystalline In_2O_3-based powders had an inflection point in the lattice parameter with increasing doping, reaching saturation at higher amounts of doping. It is therefore inferred that the nano-crystalline powders also have secondary phases above this concentration, but with amounts and/or crystallite sizes too small to be observed by XRD. The broadened reflections due to the nano-crystalline nature of the powders make it more difficult to detect small amounts of secondary phases. Furthermore, the nano-crystalline powders had a larger lattice parameter than their sintered counterparts, except for the nano-crystalline powders with large amounts of Tb, as discussed above. The increase in the lattice parameter is proposed to be caused by a finite size effect, due to the nano-scale nature of the powder.

Functional properties

A dramatic decrease in the conductivity of the sintered In_2O_3-based materials with increasing REE-doping was demonstrated, even at low doping concentrations (Fig. 5 (a)). The decrease was most significant for In_2O_3:Nd and progressively smaller for In_2O_3:Eu and In_2O_3:Tb. There appears to be a correlation between the size of the dopant and the decrease in the conductivity. The thermopower of the materials, on the other hand, was not affected by the REE-doping (Fig. 5 (b)). While the conductivity is a function of both charge mobility and carrier concentration, the thermopower only varies with carrier concentration.[33] If the reduction in the conductivity was caused by a decrease in the charge carrier concentration, a similar response would have been observed in the thermopower of the materials. Hence, the dramatic decrease in conductivity for In_2O_3 doped with REEs must be caused by a decrease in mobility. It is reasonable that the REE-dopants, which are isovalent with In^{3+}, should not cause a dramatic decrease in the carrier concentration. The materials with low doping concentration were all phase-pure (small traces of secondary phase was observed for In_2O_3:1%Nd), suggesting that the decrease in mobility is not caused by the presence of secondary phases. A possible explanation is that the exposure to high temperatures caused the dopants to segregate to the grain boundaries of the sample, possibly forming Schottky barriers or alternatively forming an amorphous or X-ray amorphous grain boundary phase. An attempt to search for an increase in REE-concentration at grain boundaries was conducted by EDS and SEM, but the concentrations obtained were too small to be conclusive. Electrical impedance spectroscopy of the materials was also performed in order to quantify the grain boundary

ARTICLE

contributions to the overall resistance, but the materials were too conductive to provide useful results. The dramatic decrease in the mobility at low doping concentrations was not observed for the thin films. The sintered materials were fired at 1400 °C, but the thin films were only annealed at 530 °C, where the cation mobility is limited. The reduced mobility due to segregation to grain boundary is therefore more likely at higher temperatures where the cation mobility is higher. Both the conductivity and the thermopower of the sintered ITO-based materials appeared to be largely unaffected by the REE-doping at low concentrations. However, the solid solubility was limited for these materials, and they were not phase-pure. The electrical properties of the ITO-based thin films remained largely unaffected by the REE-doping. The carrier concentrations in the materials are dominated by the active n-type tin-donors in the material. This explains why the properties are largely unaffected, and also why there is a slight increase in the sheet resistance at 10 cat% Eu-doping due to reducing the tin-concentration from 5 to 4.5 cat%. The electrical properties of both the In_2O_3- and the ITO-based thin films were not significantly affected at low doping concentrations, which is reasonable as the REE-dopants are isovalent with In^{3+}. In contrast to the ITO-based thin films, the properties of the In_2O_3-based thin films changed dramatically at high Eu-doping concentrations. This is most likely related to interactions of the dopant species with the intrinsic oxygen vacancy donors, which are known to be responsible for carrier generation in undoped indium oxide.[67]

The In_2O_3:Eu materials exhibited a broad emission centred around 611 nm upon excitation at 465 and 530 nm. The emission is attributed to the transition $^5D_0 \rightarrow$ $^7F_2$, while the excitations corresponds to transitions from the ground state of Eu^{3+}, $^7F_0$, to the levels $^5D_2$ and $^5D_1$.[11] The emission was fairly broad, which has been attributed to the activator not being well incorporated into the host lattice.[11] However, the lattice parameters clearly increased with increasing amount of doping, as shown in Fig. 2 (b), thereby pointing towards homogenous incorporation of the dopants. The lower intensity emissions at approximately 578, 584, 592, 597 and 629 nm are ascribed to transitions from $^5D_0$ to $^7F_0$, $^7F_1$ and $^7F_2$ levels.[11] The absence of excitations at lower wavelengths indicates that host sensitisation was not possible and that emissions only occurred upon direct excitation of the 4f energy levels of Eu^{3+}. This is in line with the work of Xiao et al. where strong host sensitisation was only observed at temperatures below 200 K, while excitation over the band gap of the host was absent at room temperature.[11] The emission at 611 nm increased in intensity with increasing Eu-doping up to 5 cat%, but then decreased for 10 cat% Eu. It is known that doping above a certain limit can cause concentration quenching of the luminescence, due to non-radiative interactions between the REE activator ions.[1] However, the material with 10 cat% Eu contained a secondary phase, which also might affect the photoluminescence. The lifetime of the 611 nm

emission after excitation at 530 nm for In_2O_3:5%Eu was 0.87 ms, which compares well with previously reported value of 0.81 ms[11] and values reported for Eu^{3+} in organic complexes.[60] The lifetime for In_2O_3:10%Eu was 0.78 ms, again illustrating the negative effect of increasing the doping concentration above a certain limit.

It was demonstrated that the sintered materials have longer lifetimes than their corresponding nano-crystalline powder materials (Table S4). The shape of the luminescence decay curves also indicated a more complicated behaviour for the powders, as seen in Fig. 9. A significant amount of the previous works focuses on nano-particles or quantum dot hosts.[11,24,27,43,44] By controlling the size of the nano-particles it could be possible to control their band gaps. This would affect where in the UV the nano-particles absorb light, and could also influence whether the energy levels of the host and activator are appropriately matched for the host sensitisation to occur.[43] However, in this work it is obvious that the sintered samples had better luminescence properties than the nano-crystalline powder. It is not clear whether this was caused by finite size effects influencing the band structure of the powder. No host sensitisation was observed, which might indicate that the match between the energy levels of the host and activator was not the limitation. A possible explanation is a better incorporation of the dopants in the lattice for the sintered materials. It is also known that OH-groups are formed on the In_2O_3 surface in the presence of water,[68] and that these groups can significantly decrease the luminescence from the REEs.[38,45] High temperatures are required to remove them,[46,69] and it is therefore possible that the nano-crystalline powders retain OH-groups on their surfaces. The nano-sized powders also have a higher surface-to-volume ratio, which is known to cause more defects, such as oxygen vacancies. However, these defects are proposed to be beneficial for the energy transfer from the host to the REE dopant,[41,44] and are therefore probably not the cause of the weaker emissions for the powders in this work. It has recently been reported that the energy transfer from In_2O_3 to Er^{3+} actually only occurred for larger sub-micron particles, and not for nano-crystalline particles of the host.[39] Whether the performance of the phosphor is better for nano-sized hosts must therefore be carefully evaluated for the specific case.

The diffuse reflectance of In_2O_3 doped with Nd clearly demonstrated absorption bands around 518, 531, 594, 630, 691, 750, 806 and 885 nm. These absorptions are ascribed to energy transitions from the ground state of Nd^{3+}, being $^4I_{9/2}$, to $^2G_{9/2}$, $^4G_{7/2}$, $^2G_{7/2}/^4G_{5/2}$, $^2H_{11/2}$, $^4F_{9/2}$, $^4F_{7/2}$, $^4F_{5/2}$ and $^4F_{3/2}$, respectively[1,70]. However, even if the materials were demonstrated to have the absorptions corresponding to the characteristic energy transitions of Nd^{3+}, it was not possible to observe the distinct emission around 1064 nm.[1] The same observations have also been made for Nd-doping of ZnO_2.[71] Nor was it possible to observe emissions in the Tb-doped materials. The cause of this absence is

unclear. However it can be speculated that the band structure of the In_2O_3 host matches more favourably with the energy levels of Eu^{3+} than Nd^{3+} and Tb^{3+}, or that energy transitions for the latter dopants can be more sensitive to non-radiative multi-phonon interactions with In_2O_3. In case of the Nd-doped materials the presence of the secondary phase could also have an effect.

Conclusions

Phase-pure and nano-crystalline powders of In_2O_3 and ITO doped with Nd, Eu and Tb were successfully prepared by an aqueous sol-gel process. The equilibrium phase composition and solid solubility of the REEs in In_2O_3 and ITO at 1400 °C were determined. The solubilites of the REEs in In_2O_3 were largely controlled by the size of the dopant, ranging from about 1 cat% for Nd to about 10 cat% for Tb, being the largest and smallest of the three dopants, respectively. When ITO was used as a host the solid solubility was greatly reduced due to a strong tendency of the tin and REE co-dopants to form a pyrochlore $RE_2Sn_2O_7$ phase. Isothermal phase diagrams for the three systems at 1400 °C were constructed based on the findings. The effect of the REE-doping on the functional properties of the host was investigated. The conductivity of sintered materials of REE-doped In_2O_3 was significantly reduced, even at low doping concentrations, due to a decrease in carrier mobility. ITO-based sintered materials did not experience the same decrease, although these materials were not phase-pure. The dramatic decrease in the mobility was not observed for thin films of the same materials. Finally, strong emissions at around 611 nm were observed for Eu-doped In_2O_3, demonstrating the possibility of obtaining photoluminescence in a TCO host material. No emissions were observed for the Nd- or Tb-doped materials, even though the characteristic absorptions due to energy transitions in Nd were observed by diffuse reflectance.

Acknowledgements

Notes and references
a Department of Materials Science and Engineering, Norwegian University of Science and Technology, N-7491 Trondheim, Norway. * E-mail: tor.grande@ntnu.no.

b Department of Physics, Norwegian University of Science and Technology, N-7491 Trondheim, Norway.

c Department of Materials Science and Engineering, Northwestern University, Evanston, Il 60208, USA.
Electronic Supplementary Information (ESI) available: The ESI contains details about the synthesis, the phase evolution after heat treatment at different temperatures, structural properties of the prepared thin films, details about the electrical and optical properties and band gaps of the materials and luminescence decay measurements.

1   A. J. Kenyon, *Prog. Quantum Electron.*, 2002, **26**, 225.

2   J. C. G. Bunzli and C. Piguet, *Chem. Soc. Rev.*, 2005, **34**, 1048.

3   J. Kido and Y. Okamoto, *Chem. Rev.*, 2002, **102**, 2357.

4   F. Wang and X. G. Liu, *Chem. Soc. Rev.*, 2009, **38**, 976.

5   A. H. Kitai, ed. in *Solid state luminescense - Theory, materials and devices*, Chapman & Hall, London, 1993.

6   M. Kawa and J. M. J. Frechet, *Chem. Mat.*, 1998, **10**, 286.

7   A. D'Aleo, A. Picot, A. Beeby, J. A. G. Williams, B. Le Guennic, C. Andraud and O. Maury, *Inorg. Chem.*, 2008, **47**, 10258.

8   C. Pitois, A. Hult and M. Lindgren, *J. Lumines.*, 2005, **111**, 265.

9   W. R. Glomm, S. Volden, J. Sjoblom and M. Lindgren, *Chem. Mat.*, 2005, **17**, 5512.

10   Y. S. Liu, W. Q. Luo, H. M. Zhu and X. Y. Chen, *J. Lumines.*, 2011, **131**, 415.

11   Q. B. Xiao, Y. S. Liu, L. Q. Liu, R. F. Li, W. Q. Luo and X. Y. Chen, *J. Phys. Chem. C*, 2010, **114**, 9314.

12   R. Kudrawiec, A. Podhorodecki, N. Mirowska, J. Misiewicz, I. Molchan, N. V. Gaponenko, A. A. Lutich and S. V. Gaponenko, *Mater. Sci. Eng., B*, 2003, **105**, 53.

13   Y. S. Liu, W. Q. Luo, R. F. Li, H. M. Zhu and X. Y. Chen, *Opt. Express*, 2009, **17**, 9748.

14   A. S. Pereira, M. Peres, M. J. Soares, E. Alves, A. Neves, T. Monteiro and T. Trindade, *Nanotechnol.*, 2006, **17**, 834.

15   Y. P. Du, Y. W. Zhang, L. D. Sun and C. H. Yan, *J. Phys. Chem. C*, 2008, **112**, 12234.

16   J. Bang, H. Yang and P. H. Holloway, *J. Chem. Phys.*, 2005, **123**, 5.

17   Y. S. Liu, W. Q. Luo, R. F. Li, G. K. Liu, M. R. Antonio and X. Y. Chen, *J. Phys. Chem. C*, 2008, **112**, 686.

18   W. Q. Luo, R. F. Li and X. Y. Chen, *J. Phys. Chem. C*, 2009, **113**, 8772.

19   J. B. Yin, L. Q. Xiang and X. P. Zhao, *Appl. Phys. Lett.*, 2007, **90**, 3.

20   W. Q. Luo, R. F. Li, G. K. Liu, M. R. Antonio and X. Y. Chen, *J. Phys. Chem. C*, 2008, **112**, 10370.

21   Z. Assefa, R. G. Haire and P. E. Raison, *Spectrochim. Acta A*, 2004, **60**, 89.

22   A. C. Yanes, J. Del Castillo, M. Torres, J. Peraza, V. D. Rodriguez and J. Mendez-Ramos, *Appl. Phys. Lett.*, 2004, **85**, 2343.

23   J. T. Kong, H. M. Zhu, R. F. Li, W. Q. Luo and X. Y. Chen, *Opt. Lett.*, 2009, **34**, 1873.

24   J. Vela, B. S. Prall, P. Rastogi, D. J. Werder, J. L. Casson, D. J. Williams, V. I. Klimov and J. A. Hollingsworth, *J. Phys. Chem. C*, 2008, **112**, 20246.

25   Y. G. Choi, S. M. Yu and W. J. Chung, *Chem. Phys. Lett.*, 2008, **461**, 290.

26   J. K. Kim and Y. G. Choi, *Thin Solid Films*, 2009, **517**, 5084.

27   D. P. Dutta, V. Sudarsan, P. Srinivasu, A. Vinu and A. K. Tyagi, *J. Phys. Chem. C*, 2008, **112**, 6781.

28   G. Adachi and N. Imanaka, *Chem. Rev.*, 1998, **98**, 1479.

29   R. D. Shannon, *Acta Crystallogr., Sect. A*, 1976, **32**, 751.

30   I. Hamberg and C. G. Granqvist, *J. Appl. Phys.*, 1986, **60**, R123.

31   C. G. Granqvist and A. Hultaker, *Thin Solid Films*, 2002, **411**, 1.

32   R. B. H. Tahar, T. Ban, Y. Ohya and Y. Takahashi, *J. Appl. Phys.*, 1998, **83**, 2631.

33   G. B. Gonzalez, T. O. Mason, J. P. Quintana, O. Warschkow, D. E. Ellis, J. H. Hwang, J. P. Hodges and J. D. Jorgensen, *J. Appl. Phys.*, 2004, **96**, 3912.

34   C. Ronda, ed. in *Luminescence: From theory to applications*, Wiley-VCH Verlag, 2008.

35   W. J. Miniscalco, *J. Lightwave Technol.*, 1991, **9**, 234.

36   E. Garskaite, M. Lindgren, M. A. Einarsrud and T. Grande, *J. Eur. Ceram. Soc.*, 2010, **30**, 1707.

37   C. C. Ting, C. H. Tsai, Y. C. Chien and C. T. Yu, *J. Electrochem. Soc.*, 2012, **159**, H400.

38   A. Podhorodecki, R. Kudrawiec, J. Misiewicz, N. V. Gaponenko and D. A. Tsyrkunov, *Opt. Mater.*, 2006, **28**, 685.

39   Q. B. Xiao, H. M. Zhu, D. T. Tu, E. Ma and X. Y. Chen, *J. Phys. Chem. C*, 2013, **117**, 10834.

40   S. Sivakumar, F. van Veggel and M. Raudsepp, *ChemPhysChem*, 2007, **8**, 1677.

41   S. Ghosh, K. Das, G. Sinha, J. Lahtinen and S. K. De, *J. Mater. Chem. C*, 2013, **1**, 5557.

42   H. K. Kim, C. C. Li, G. Nykolak and P. C. Becker, *J. Appl. Phys.*, 1994, **76**, 8209.

43   N. Wan, J. Xu, T. Lin, X. G. Zhang and L. Xu, *Appl. Phys. Lett.*, 2008, **92**, 3.

44   Y. L. Yu, D. Q. Chen, Y. S. Wang, P. Huang, F. Y. Weng and M. T. Niu, *Phys. Chem. Chem. Phys.*, 2009, **11**, 8774.

45   T. Lin, X. Y. Ding, J. Xu, N. Wan, L. Xu and K. J. Chen, *J. Appl. Phys.*, 2011, **109**,

46   T. O. L. Sunde, E. Garskaite, B. Otter, H. E. Fossheim, R. Saeterli, R. Holmestad, M. A. Einarsrud and T. Grande, *J. Mater. Chem.*, 2012, **22**, 15740.

47   M. Marezio, *Acta Crystallogr.*, 1966, **20**, 723.

48   C. G. Whinfrey, D. W. Eckart and A. Tauber, *J. Am. Chem. Soc.*, 1960, **82**, 2695.

49   B. J. Kennedy, B. A. Hunter and C. J. Howard, *J. Solid State Chem.*, 1997, **130**, 58.

50   S. J. Schneider, R. S. Roth and J. L. Waring, *J. Res. Natl. Bur. Stand.*, 1961, **A 65**, 345.

51   D. M. Giaquinta and H. C. Zurloye, *Chem. Mat.*, 1994, **6**, 365.

52   R. D. Shannon, *Inorg. Chem.*, 1967, **6**, 1474.

53   C. Pistorius and G. J. Kruger, *J. Inorg. Nucl. Chem.*, 1976, **38**, 1471.

54   B. S. Hong, S. J. Ford and T. O. Mason, in *Equilibrium electrical property measurements in electroceramics*, Trans Tech Publications Ltd, Stafa-Zurich, 1997.

55   F. M. Smits, *Bell Syst. Tech. J.*, 1958, **37**, 711.

56   D. S. McLachlan, M. Blaszkiewicz and R. E. Newnham, *J. Am. Ceram. Soc.*, 1990, **73**, 2187.

57   L. J. van der Pauw, *Applied Physics a-Materials Science & ProcessingJournal of Physical and Chemical Reference Data*, 1958, **20**, 220

58   L. Vegard, *Z. Phys.*, 1921, **5**, 17.

59   G. Frank and H. Kostlin, *Appl. Phys. A*, 1982, **27**, 197.

60   P. Antoni, M. Malkoch, G. Vamvounis, D. Nystrom, A. Nystrom, M. Lindgren and A. Hult, *J. Mater. Chem.*, 2008, **18**, 2545.

61   C. L. Heng, T. G. Finstad, P. Storas, Y. J. Li, A. E. Gunnaes and O. Nilsen, *Appl. Phys. Lett.*, 2004, **85**, 4475.

62   G. B. Gonzalez, J. S. Okasinski, T. O. Mason, T. Buslaps and V. Honkimaeki, *J. Appl. Phys.*, 2008, **104**,

63   G. B. Gonzalez, T. O. Mason, J. S. Okasinski, T. Buslaps and V. Honkimaki, *J. Am. Ceram. Soc.*, 2012, **95**, 809.

64   W. J. Heward and D. J. Swenson, *J. Mater. Sci.*, 2007, **42**, 7135.

65   D. M. Gruen, W. C. Koehler and J. J. Katz, *J. Am. Chem. Soc.*, 1951, **73**, 1475.

66   S. Stølen and T. Grande, in *Chemical thermodynamics of materials*, John Wiley & Sons, London, 2004.

67   J. H. W. De Wit, *J. Solid State Chem.*, 1977, **20**, 143.

68   M. Brumbach, P. A. Veneman, F. S. Marrikar, T. Schulmeyer, A. Simmonds, W. Xia, P. Lee and N. R. Armstrong, *Langmuir*, 2007, **23**, 11089.

69   G. Korotcenkov, V. Brinzari, J. R. Stetter, I. Blinov and V. Blaja, *Sens. Actuators, B*, 2007, **128**, 51.

70   P. W. France, M. G. Drexhage, J. M. Parker, M. W. Moore, S. F. Carter and J. V. Wright, in *Fluoride glass optical fibres*, Blackie, Glasqow, 1990.

71   J. Kossanyi, D. Kouyate, J. Pouliquen, J. C. Ronfardharet, P. Valat, D. Oelkrug, U. Mammel, G. P. Kelly and F. Wilkinson, *J. Lumines.*, 1990, **46**, 17.

72   T. O. L. Sunde, M. A. Einarsrud and T. Grande, *J. Eur. Ceram. Soc.*, 2013, **33**, 565.

Table 1 The composition and label of the materials discussed in this work. RE = Nd, Eu or Tb.

Material label	Nominal composition	cat% In	cat% Sn	cat% RE
In_2O_3	In_2O_3	100	-	-
ITO	$In_{1.9}Sn_{0.1}O_3$	95	5	-
In_2O_3:RE	$In_{1.99}RE_{0.01}O_3$	99.5	-	0.5
	$In_{1.98}RE_{0.02}O_3$	99	-	1
	$In_{1.96}RE_{0.04}O_3$	98	-	2
	$In_{1.9}RE_{0.1}O_3$	95	-	5
	$In_{1.8}RE_{0.2}O_3$	90	-	10
ITO:RE	$In_{1.881}Sn_{0.099}RE_{0.02}O_3$.	94.05	4.95	1
	$In_{1.805}Sn_{0.095}RE_{0.1}O_3$	90.25	4.75	5
	$In_{1.71}Sn_{0.09}RE_{0.2}O_3$	85.5	4.5	10

Journal Name   RSCPublishing

Table 2 The lattice parameter for the cubic In$_2$O$_3$ phase, the crystallite size and phase content obtained by Rietveld refinement for In$_2$O$_3$ doped with different amounts of Nd, Eu and Tb for nano-crystalline powder after calcination at 600 °C and materials after sintering at 1400 °C. The estimated uncertainty is ± 0.002 and 0.001 Å in the lattice parameter for the powders and the sintered materials, respectively, and ± 3 nm for the crystallite size and ± 1 wt % for the phase content.

| Dopant | Doping amount [cat%] | Nano-crystalline powders, 600 °C | | Sintered materials, 1400 °C | | | Goodness of Rietveld fit [R$_{wp}$] |
		Lattice parameter [Å]	Crystallite size [nm]	Lattice parameter [Å]	In$_2$O$_3$ [wt%]	REInO$_3$ [wt%]	
Nd	0.5	10.133	22	10.122	100.0	-	12.5
	1	10.147	20	10.125	~100.0	traces	8.4
	2	10.143	18	10.125	97.4	2.6	7.6
	5	10.142	18	10.124	90.5	9.5	7.4
	10	10.145	18	10.126	79.0	21.0	6.4
Eu	0.5	10.133	22	10.121	100.0	-	8.1
	1	10.132	20	10.124	100.0	-	9.3
	2	10.144	18	10.134	100.0	-	8.1
	5	10.159	18	10.156	~100.0	traces	7.1
	10	10.161	17	10.155	93.1	6.9	7.0
Tb	0.5	10.132	23	10.120	100.0	-	8.1
	1	10.140	19	10.125	100.0	-	6.5
	2	10.136	20	10.129	100.0	-	7.8
	5	10.142	19	10.151	100.0	-	7.2
	10	10.155	18	10.185	~100.0	traces	5.7

Table 3 The lattice parameter for the cubic In_2O_3 phase, the crystallite size and phase content obtained by Rietveld refinement for ITO doped with different amounts of Nd, Eu and Tb for nano-crystalline powders after calcination at 600 °C and materials after sintering at 1400 °C. The estimated uncertainty is ± 0.002 and 0.001 Å in the lattice parameter for the nano-crystalline powders and the sintered materials, respectively, and ± 3 nm for the crystallite size and ± 1 wt % for the phase content.

Dopant	Doping amount [cat%]	Nano-crystalline powder, 600 °C		Sintered material, 1400 °C				
		Lattice parameter [Å]	Crystallite size [nm]	Lattice parameter [Å]	In_2O_3 [wt%]	$RE_2Sn_2O_7$ [wt%]	$REInO_3$ [wt%]	Goodness of Rietveld fit [R_{wp}]
Nd	1	10.139	21	10.122	96.9	3.1	-	7.2
	5	10.138	18	10.128	89.9	10.1	-	5.9
	10	10.148	23	10.126	78.7	8.7	12.6	5.8
Eu	1	10.128	22	10.125	97.2	2.8	-	7.2
	5	10.141	23	10.131	90.5	9.5	-	7.0
	10	10.150	24	10.148	87.5	9.9	2.6	7.7
Tb	1	10.134	22	10.124	97.9	2.1	-	10.4
	5	10.130	23	10.132	90.7	9.3	-	9.5
	10	10.157	20	10.162	~89.9	~10.1	traces	6.7

Journal Name

ARTICLE

Table 4 Estimated composition of the cubic In_2O_3 phase sintered materials of ITO doped with Nd, Eu and Tb based on mass balance and the lever rule.

Material	Nominal composition [cat%]			Composition of cubic In_2O_3 [cat%]		
	In	Sn	RE	In	Sn	RE
ITO:1%Nd	94.1	4.9	1.0	96.1	3.9	0.0
ITO:5%Nd	90.3	4.7	5.0	98.0	1.1	0.9
ITO:10%Nd	85.5	4.5	10.0	98.3	0.9	0.8
ITO:1%Eu	94.1	4.9	1.0	96.0	4.0	0.0
ITO:5%Eu	90.3	4.7	5.0	97.2	1.4	1.4
ITO:10%Eu	85.5	4.5	10.0	94.0	1.3	4.7
ITO:1%Tb	94.1	4.9	1.0	95.8	4.2	0.0
ITO:5%Tb	90.3	4.7	5.0	97.2	1.5	1.3
ITO:10%Tb	85.5	4.5	10.0	93.0	1.0	6.0
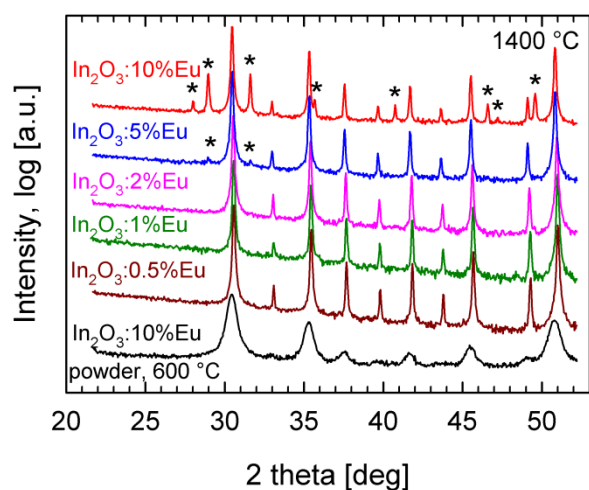
Fig. 1 XRD patterns of In$_2$O$_3$ doped with different amounts of Eu after heat treatment at 1400 °C. Diffraction lines from EuInO$_3$ are denoted by *. The bottommost diffractogram is for In$_2$O$_3$:10% Eu powder after calcination at 600 °C.
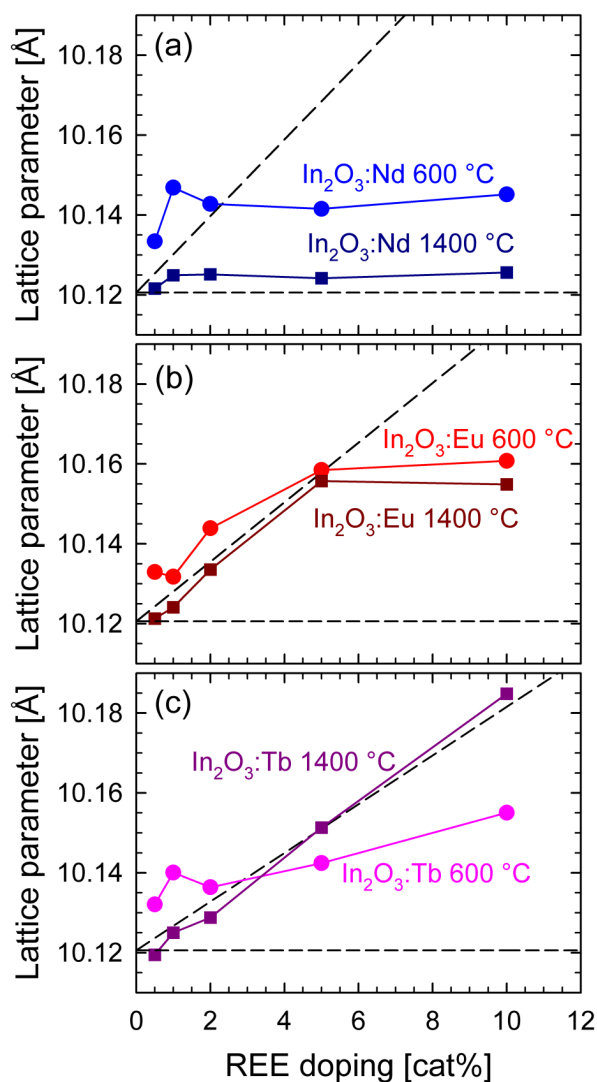
Fig. 2 Lattice parameters of cubic In$_2$O$_3$ doped with Nd (a), Eu (b) and Tb (c) in nano-crystalline powders after calcination at 600 °C (●) and in materials after sintering at 1400 °C (■). The horizontal dashed lines are lattice parameters of undoped In$_2$O$_3$ (10.1207 Å) powders.[46] The diagonal dashed lines are the predicted lattice parameter changes according to Vegard's law with end values of 11.0770, 10.8660 and 10.7300 Å for Nd$_2$O$_3$, Eu$_2$O$_3$ and Tb$_2$O$_3$, respectively.[28]
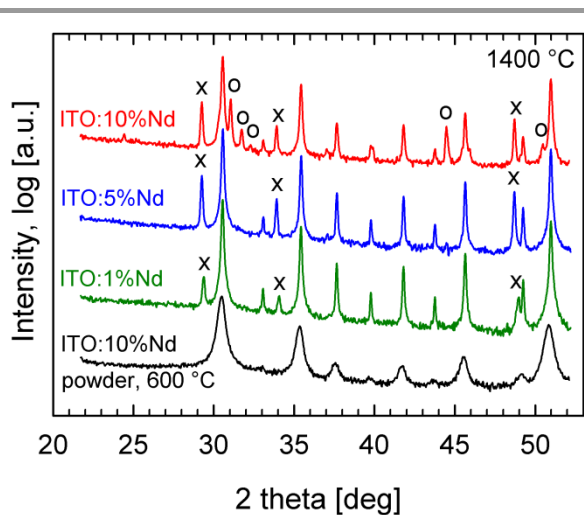
Fig. 3 XRD patterns of ITO doped with different amounts of Nd for nano-crystalline powders after calcination at 600 °C and materials sintered at 1400 °C. Diffraction lines from $Nd_2Sn_2O_7$ are marked by "X" and from $NdInO_3$ by "O".
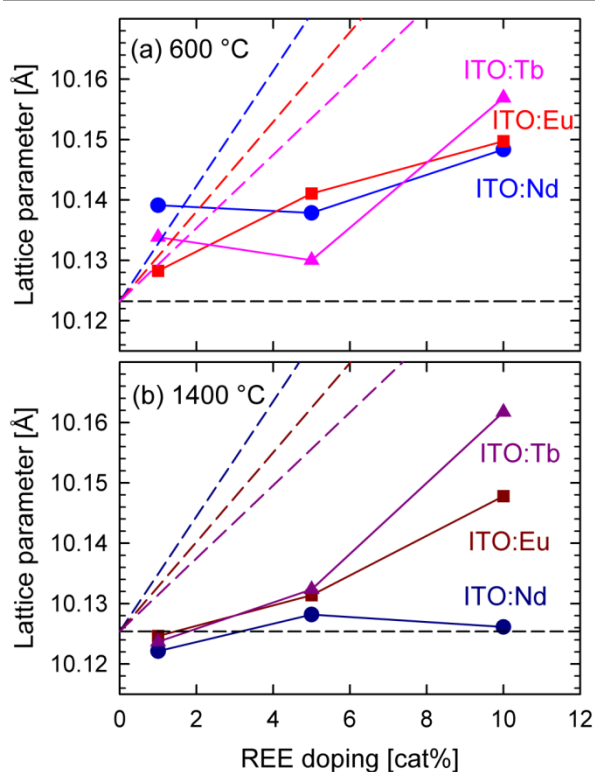
Fig. 4 Lattice parameters of the cubic In_2O_3 phase in ITO doped with Nd (●), Eu (■) and Tb (▲), for nano-crystalline powders calcined at 600 °C (a), and materials sintered at 1400 °C (b). The horizontal dashed lines are the lattice parameter of ITO (10.1233 Å for the powder[46] and 10.1254 Å for the sintered material[72]). The diagonal dashed lines are the predicted lattice parameter changes according to Vegard's law with end values of 11.0770, 10.8660 and 10.730 Å for Nd_2O_3, Eu_2O_3 and Tb_2O_3, respectively.[28]

Dalton Transactions Accepted Manuscript

Journal Name

ARTICLE
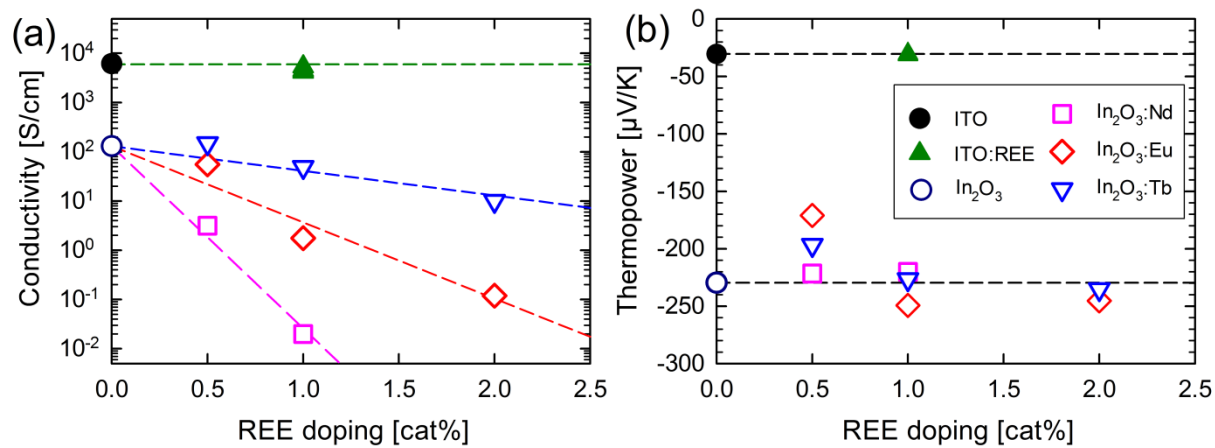
Fig. 5 Conductivity (a) and thermopower (b) of sintered materials of In_2O_3 and ITO doped with Nd, Eu and Tb. The dashed lines are guides to the eye. The same labelling is used in both figures.
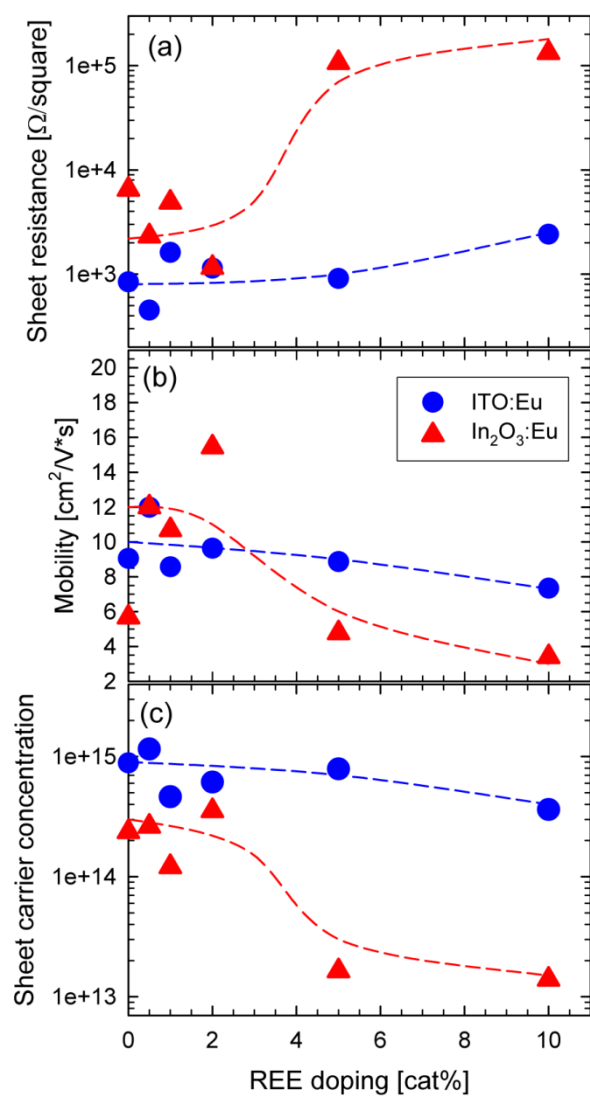
Fig. 6 Sheet resistance (a), mobility (b) and sheet carrier concentration (c) of ITO:Eu (●) and In2O3:Eu (▲). The same labelling is used in the three figures. The dashed lines are guides to the eye.
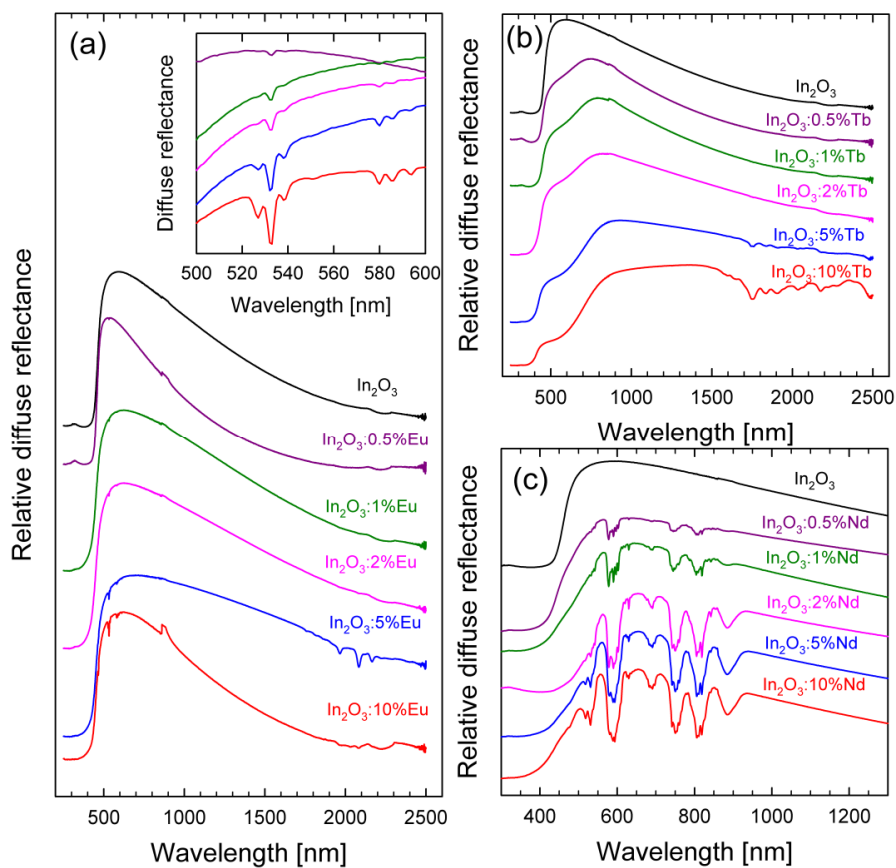
Fig. 7 Diffuse reflectance of sintered In_2O_3-based materials with different amounts of Eu- (a), Tb- (b) and Nd-doping (c). The inset in (a) shows a close-up of the absorptions around 530 and 580 nm with the topmost material being In_2O_3:0.5%Eu and the bottommost In_2O_3:10%Eu. The anomaly at 860 nm is due to a change of detector.

Journal Name

ARTICLE
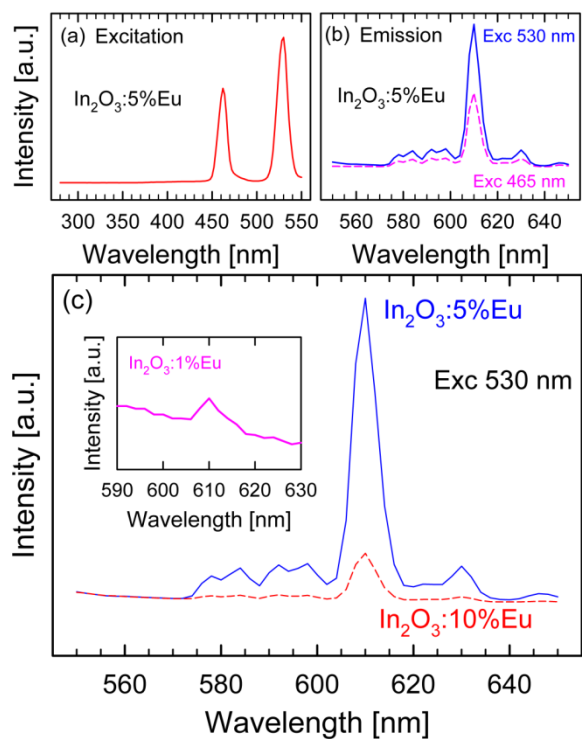
Fig. 8 Photoluminescence excitation and emission spectra of sintered materials of In_2O_3 doped with Eu. (a) Excitation spectra of In_2O_3:5%Eu while monitoring the emission at 611 nm. (b) Emission spectra of In_2O_3:5%Eu after excitation at 530 (solid line) and 465 nm (broken line). (c) Emission spectra of In_2O_3:5%Eu (solid line) and In_2O_3:10%Eu (broken line) after excitation at 530 nm. The inset shows a similar emission spectrum for In_2O_3:1%Eu.
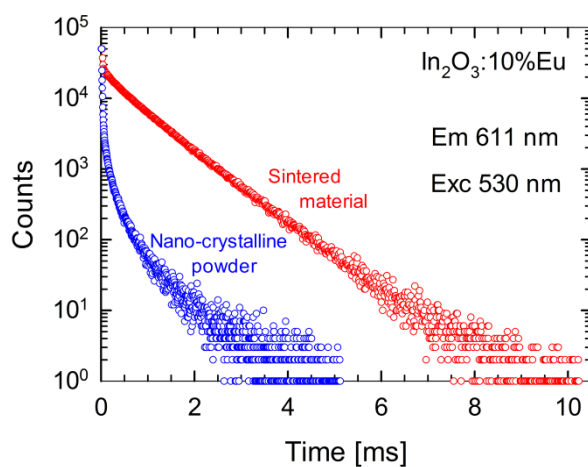
Fig. 9 Luminescence decay curves of the 611 nm emission for nano-crystalline powder calcined at 600 °C and material sintered at 1400 °C of In_2O_3:10%Eu after excitation at 530 nm. The solid lines are the fit obtained using three exponential decays for the nano-crystalline powder and two for the sintered material.
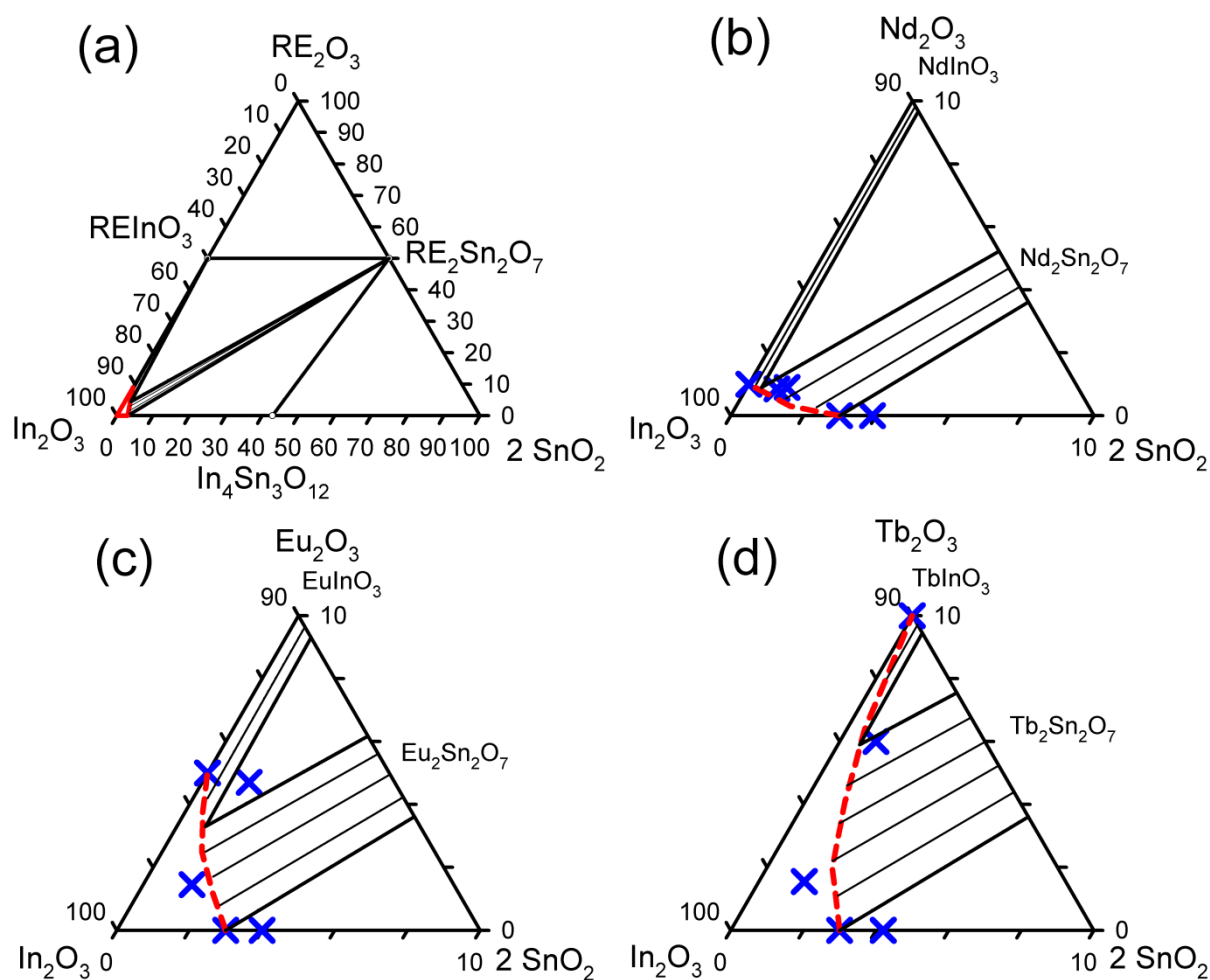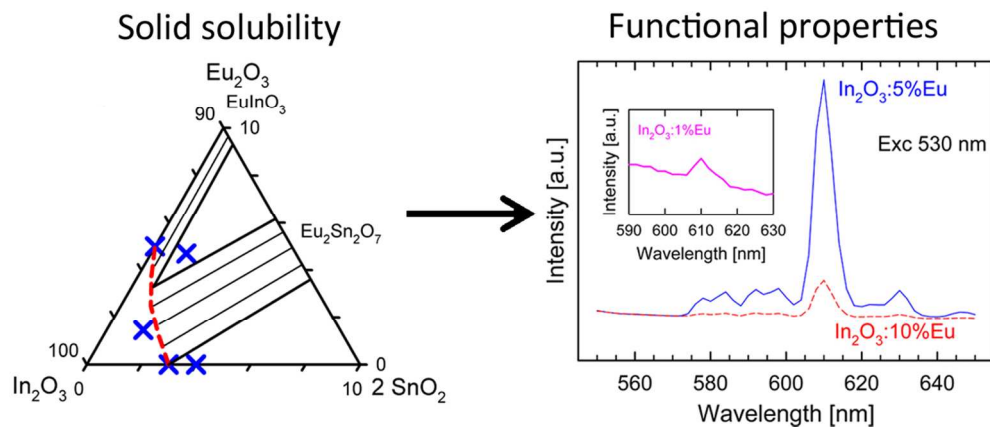
Fig. 10 Ternary phase diagram of the system In_2O_3-SnO_2-RE_2O_3 at 1400 °C (a). The solid solubility region of the indium-rich phase in the bottom left corner is marked with bold red lines. Close up of the indium-rich corner of the ternary phase diagrams of the systems In_2O_3-SnO_2-RE_2O_3 with RE_2O_3 = Nd_2O_3 (b), Eu_2O_3 (c) and Tb_2O_3 (d) at 1400 °C. The crosses marks the composition of the In_2O_3 phase in the ITO materials with 1, 5 and 10 cat% REE-doping, as given in Table 4, and the solid solubility of RE and Sn in In_2O_3. The proposed solid solubility region of In_2O_3 is marked with a broken line. The thinner lines represent two phase regions.

444x188mm (72 x 72 DPI)